Binding Site Recognition and Docking Dynamics of a Single Electron Transport Protein: Cytochrome c_2

Abhishek Singharoy[†], **Angela M. Barragan**[†,‡,§], **Sundarapandian Thangapandian**[†,§], **Emad Tajkhorshid**[†,¶], and **Klaus Schulten**[*,†,‡]

[†]Beckman Institute for Advanced Science and Technology, University of Illinois at Urbana–Champaign, 405 N. Mathews Ave., Urbana, IL 61801, USA

[‡]Department of Physics, University of Illinois at Urbana–Champaign, 1110 W. Green St., Urbana, IL 61801, USA

[¶]Department of Biochemistry, University of Illinois Urbana–Champaign, 600 S. Mathews Ave., Urbana, IL 61801, USA

Abstract

Small diffusible redox proteins facilitate electron transfer in respiration and photosynthesis by alternately binding to their redox partners, integral membrane proteins, and exchanging electrons. Diffusive search, recognition, binding and unbinding of these proteins amount often to kinetic bottlenecks in cellular energy conversion, but despite the availability of structures and intense study, the physical mechanisms controlling redox partner interactions remain largely unknown. The present molecular dynamics study provides an all-atom description of the cytochrome c_2 - docked bc_1 complex in *Rhodobacter sphaeroides* in terms of an ensemble of favorable docking conformations, and reveals an intricate series of conformational changes that allow cytochrome c_2 to recognize the bc_1 complex and bind or unbind in a redox state-dependent manner. In particular, the role of electron transfer in triggering a molecular switch, and in altering water-mediated interface mobility, thereby strengthening and weakening complex formation, is described. The results resolve long-standing discrepancies between structural and functional data.

Introduction

Cellular respiratory and photosynthetic pathways employ small diffusible redox proteins for the transport of single electrons between neighboring, as well as widely separated, membrane-integrated enzymatic complexes. The proteins are required as single electrons must be moved between different parts of the bioenergetic apparatus which can be achieved only by special redox proteins, not by small molecules as the latter are converted through transfer of single electrons to chemical radicals that cannot be turned loose in the cell.

[*]To whom correspondence should be addressed kschulte@ks.uiuc.edu.
[§]Contributed equally to this work

Cytochrome c (cyt. c) is one such single electron transport protein capable of safeguarding a single electron. Cyt. c belongs to an exemplary family of redox proteins that participate in the mitochondrial electron transport chain, shuttling electrons, usually only over a short distance, between the cytochrome bc_1 complex and cytochrome c oxidase.[1–3] Similarly, cytochrome c_2 (cyt. c_2), a homologue of mitochondrial cyt. c, mediates membrane-wide electron transport between bc_1 complex and reaction center proteins within the chromatophore,[4,5] a vesicle-shaped photosynthetic apparatus found in purple bacteria.

To carry out their function single electron transport proteins need to find and dock to the electron donor, transfer the electron and unbind as a result of it, and afterwards find the electron acceptor, dock to it to deliver the electron and unbind to repeat the sequence. In the present computational study we seek to determine, for the case of cyt. c_2 docking to the cyt. c_1 subunit of the bc_1 complex, the recognition, docking and undocking steps. In particular, we seek to determine the dependence of docking and undocking on the redox states of the associated cyt. c_2 and cyt. c_1 heme groups. Given that cyt. c family of electron transfer proteins from human, horse, pig, rabbit, chicken, tuna, yeast, and bacteria are highly identical in terms of structure and sequence,[1,2] our study of the *Rhodobacter* (*Rba.*) *sphaeroides* photosynthetic system applies to electron transfer mediated by cyt. c in respiratory processes and cyt. c_2 in photosynthetic processes.

To illustrate the specific role of cyt. c_2 in the photosynthesis of purple bacteria, energy conversion processes within the bacterial chromatophore are depicted in three stages[4] (see Fig. S1). In the first stage, light energy is absorbed and transferred to the photosynthetic reaction center (RC), where each excitation induces a charge separation process. Two such processes, along with concomitant proton transfers, doubly reduce a quinone molecule to a quinol. In the second stage, the quinol is released from RC and joins a quinol/quinone pool; this pool delivers a quinol to a bc_1 complex. At the bc_1 complex, an iron-sulfur protein (ISP) extracts the first electron from the bound quinol (the second electron enters a separate reaction, the Q-cycle[4,5]), moves it to the heme of cyt. c_1 and, subsequently, to the heme of cyt. c_2 (Fig. 1a). The reduced cyt. c_2 unbinds from the bc_1 complex, diffuses to an electron-deficient RC, and adds back the electron. Removal of electrons from the bc_1 complex-bound quinol through cyt. c_2 and through a second electron transfer towards the Q-cycle components[4,5] yields a quinone as well as releases two protons into the periplasmic space (into the inside) of the chromatophore vesicle, thereby generating a proton gradient across the membrane. The quinone joins the quinol/quinone pool which contributes a fresh quinone to a RC, thus closing the loop. In the third stage, the proton gradient generated at the bc_1 complex is harnessed by ATP synthase to produce ATP.

An enzymatic activity of a bc_1 complex of 40 cyt. c_2 per second is essential for continuous flow of electrons during the second stage of the bacterial photosynthetic pathway described here.[6–8] Thus, the average cyt. c_2 turnover time is expected to be of the order of 25 ms. Rate measurements[8] infer that, within this 25 ms, cyt. c_2 spends 11.5 ms at the bc_1 complex surface for binding, accepting an electron and unbinding, and 1.25 ms at the RC surface for binding, donating an electron and unbinding; the remaining 12 ms are spent on traversing between bc_1 and RC while also avoiding redox-incompatible binding sites.[8] Accomplishment of such precise functions every 25 ms necessitates cyt. c_2 binding to the

bc_1 complex to be both specific and transient.[9,10] Based on salinity-profiling[11,12] and mutational studies,[13] the two characteristics of cyt. c_2 binding were hypothesized to originate from electrostatic association with the binding partners, such as cyt. c_1,[13,14] cyt. c-oxidase,[15] and RC complexes.[16] Consequently, the electrostatic interactions between cyt. c/c_2 and its binding partners have been studied in regard to their role in molecular recognition.[17] More recent crystallographic studies pointed also to a key role of hydrophobic interactions in stabilizing the cyt. c_2 interface.[10] In particular, hydrophobic interactions were found to control inter-heme distance and orientation and, thereby, electron transfer between the binding partners[9][18].

Taken together, the correct balance between, on the one hand, adhesive interactions that maintain a tight cyt. c_2 - bc_1 complex interface permiting direct inter-heme electron transfer and, on the other hand, interactions that allow separation after electron transfer, has been a subject of active debate.[10,14,19–22] For example, if the interface-stabilizing interactions were solely based on electrostatic interactions (e.g. salt bridges), unbinding of cyt. c_2 would be energetically uphill, slowing down the overall photosynthetic cycle and, thereby, the rate of ATP synthesis.[8] Cation-π interactions, on the other hand, are suggested to be present and mediate electron transfer.[9,10] However, the extent of stabilization that such interactions provide to the interface remains questionable given conflicting experimental estimates of associated energetics.[20] Thus, the cation-π interactions seem to also not be adequate for sculpting interface conformations to allow electron transfer, even though they enable a fairly transient interface as compared to an electrostatic-only binding scenario.[14] Altogether, resolution of such conceptually intriguing questions on interface recognition, binding, and unbinding, raised across a diverse range of experimental observations,[9,10,20] calls for an atomic-scale investigation of the cyt. c_2 - bc_1 binding interface.

In the present study, rigid-body docking computations are combined with molecular dynamics (MD) simulations to investigate the redox dependent binding interface between cyt. c_2 and bc_1 complex of *Rba. sphaeroides* (Fig. 1). Since the respective mitochondrial electron transfer process has been well-studied, e.g., in yeast,[9,10,23] the current *Rba. sphaeroides* results can be benchmarked against those in yeast. Notions such as half-ring guided interface recognition and docking,[14] minimal core mediated electron transfer,[10] and mobility-mismatch induced undocking,[9,14] that were hypothesized based on stationary structures for the yeast cyt. c_2 - bound bc_1 complex, are found to establish indeed a mechanism of cyt. c/c_2 binding. However, a surprising finding of the present molecular dynamics study is that a well defined cyt. c_2 - cyt. c_1 complex is not formed; rather an ensemble of nearly identical, yet conformationally slightly disordered complexes is formed that all exhibit a short heme edge-heme edge distance of 8.5 Å (Fig. 1b). This distance and the hydrophobic characteristics of the near-heme contact area is optimal for fast electron transfer. Accordingly, formation of a specific complex is neither needed nor desirable as a broad range of docking conformations are equally functional and the availability of many good states (see Fig. 1b) speeds up the recognition and binding reaction. This finding is in stark contrast to expectations from crystallographically observed structures that are interpreted to suggest the existence of single, structurally well defined docking complexes.

Another key finding is the realization of a trade-off between electrostatic, van der Waals, and cation-π interactions that modifies the binding interface as a result of cyt. $c_1 \rightarrow$ cyt. c_2 electron transfer. In particular, changes in side-chain conformation of interface residues in response to the electron transfer alter strong cyt. c_2 binding (before electron transfer) to unbinding (after electron transfer).

Clearly, critical to the answer to questions on cyt. c_2 docking dynamics is a knowledge of the bacterial cyt. c_2 - bound bc_1 complex, for which no crystallographic structure is currently available. Even the best resolved crystal structure of *Rba. sphaeroides* bc_1 complex does not include a bound cyt. c_2.[24] This gap in structural information has motivated docking studies of the *Rba. capsulatus* cyt. c_2 - bc_1 complex,[25] co-crystallization of cyt. c_2 - RC complex,[16] and simulations of electrostatic properties[26] and the dynamics of water molecules therein.[27] In the absence of experimental data our computational model provides a valuable means to achieve a comprehensive description of cyt. c_2 - bc_1 complex recognition, binding and unbinding. The study inspires similar investigations for functionally similar, yet structurally disparate, single electron transport complexes such as cytochrome c - RC, cytochrome c - cytochrome c oxidase and plastocyanin-cytochrome f complexes.

Methods

Computational protocols for modeling and simulation of the cyt. c_2 - bound bc_1 complex are outlined in this section. First, we outline the rigid-body conformational search protocols for docking cyt. c_2 onto the cyt. c_1 subunit of the bc_1 complex. We then outline the MD simulation procedures that were used to refine the docked model further and to characterize the dynamical structure of the cyt. c_2 - cyt. c_1 interface via calculations of its contact area, surface fluctuation, water content, interaction energy, and dissociation constant. Finally, we outline how steered MD simulations were employed to capture the millisecond-scale processes of cyt. c_2 binding/unbinding. More detailed descriptions of the simulation protocols adopted for the present study are provided in Section S1 of Supplementary Information (SI).

Protein-protein docking

The docking program DOT 2.0[28] was employed to construct models of the cyt. c_2 - bound bc_1 complex. DOT performs a systematic translational and rotational search of a rigid body about another one. Within our conformational search, the bc_1 complex (PDBID: 2QJY[24]) was held stationary while cyt. c_2 (PDBID: 1L9B[16]) was allowed to move. Altogether, 382 billion configurations were tested to obtain an initial set of the 2000 most optimally docked cyt. c_2 conformations. Subsequently, following a cycle of re-scoring, based on electrostatic and solvation potentials, the docked cyt. c_2 - bc_1 complex model with the closest inter-heme proximity and most favorable interaction energy was chosen for further optimization and characterization through MD simulations.

Modeling and molecular dynamics simulation

The Membrane Builder[29–31] tool of CHARMM-GUI (http://www.charmm-gui.org)[32,33] was employed to embed the optimally docked cyt. c_2 - bc_1 complex within a POPC membrane,

to build a water box around the membrane, and to add ions for neutralizing the system. The fully solvated and ionized system contained 0.5 million atoms. An identical modeling protocol was followed to prepare four systems with all possible redox states of the cyt. c_2 and cyt. c_1 hemes, referred to as $c_2^O c_1^R$ (pre-electron transfer, pre-ET), $c_2^O c_1^O$, $c_2^R c_1^R$ and $c_2^R c_1^O$ (post-electron transfer, post-ET); superindices O and R imply oxidized and reduced states of the respective heme groups. Also, two isolated cyt. c_2 in the oxidized and reduced state, denoted as c_2^O and c_2^R, were solvated and ionized. Each of the six systems were simulated for 150 ns with NAMD 2.11[34] following protocols detailed in SI. All simulations carried out for this study are listed in Table S1.

Standard CHARMM27[35] and CHARMM36[36] parameters were employed for proteins and lipids, respectively. Fe_2S_2 cluster and hemes topologies and parameters were taken from Autenrieth et al.[37] The topology and parameters of lysine and tetramethylammonium, available in CHARMM27, were employed to represent trimethylated lysine of cyt. c (M3Lys). All structural analysis of the MD simulations were performed with VMD,[38] as detailed in the SI Methods.

Steered MD simulations

To induce undocking of cyt. c_2 from the bc_1 complex we performed a set of ten 50-ns steered MD (SMD) simulations[39–41] for the pre- and post-ET states employing distance-based collective variables between center of masses of cyt. c_1 of bc_1 complex and cyt. c_2. SMD simulations were necessary, as the timescale of spontaneous cyt. c_2 unbinding is beyond the reach of atomistic MD simulations. The entire study involved a simulation time of 150 ns $\times$ 6 for MD calculations and of 50 ns $\times$ 10 for SMD calculations, altogether 1.4 μs.

Results

In the following, first, structural details of the docked cyt. c_2 - bc_1 complex model are reported. Next, the model is refined using MD simulations for four different heme redox states that are encountered during the membrane-wide cyt. c_2 transport. Side-chain conformations and solvent dynamics at the cyt. c_2 - cyt. c_1 interface are monitored in response to variations of the heme redox states. Finally, SMD simulations were performed to investigate the energetically favorable docking and undocking pathways of cyt. c_2.

Rigid-body docking of the cyt. c_2 to bc_1 complex reveals first details of the pre-ET binding interface

First, some salient features of the cyt. c_2 - cyt. c_1 complex are reported (summarized in Table S2). The binding interface is characterized by electrostatic interactions, of magnitude −21.7 kcal/mol, between positively charged residues of cyt. c_2 and negatively charged residues of cyt. c_1 (Fig. 2a). The contact area of the optimal cyt. c_2 - cyt. c_1 interface is found to be 956 Å^2. This area is smaller than a typical protein-protein interface area (~1600 $\pm$ 400 Å^2),[42] but similar to the areas seen in homologous electron-transfer complexes in yeast such as 880 Å^2 and 932 Å^2 for the cyt. c - cyt. c_1 complex in *Saccharomyces cerevisiae* in different redox states.[9,10] Also, the contact area of the optimal cyt. c_2 - cyt. c_1 complex remains in the range of those from functionally related, yet structurally dissimilar, electron-transfer complexes

with areas of 1270 Å^2 for the cyt. c_2 - RC complex in *Rba. sphaeroides*,[43] or 1200 Å^2 for the plastocyanin-cytochrome f complex in *Phormidium laminosum*.[44] Altogether, the optimal cyt. c_2 - bc_1 complex, characterized by a high docking score, complementary binding surfaces, and a contact area comparable with areas of relevant crystallographic structures, should provide a satisfactory starting point for MD studies to be described now.

MD simulation suggests a stable and functional, yet fuzzy $c_2^O c_1^R$ complex

We carried out an MD simulation of the optimal cyt. c_2 - bc_1 complex in the redox state $c_2^O c_1^R$, as described in SI Methods. The complex remained stable and exhibited a close (8.5 Å edge-edge) distance between the cyt. c_2 and cyt. c_1 heme groups, but nevertheless exhibited a fuzzy geometry characterized through an ensemble of conformations as seen in the scatter plot shown in Fig. 1b. The majority of these conformations enable fast cyt. $c_1 \rightarrow$ cyt. c_2 electron transfer, i.e., can be considered functional single-electron transfer complexes. In light of the observation of a fuzzy, namely conformationally distributed, functional $c_2^O c_1^R$ complex, rather than a functional complex with a sharp distribution, we will characterize in the following sections the interface properties of the $c_2^O c_1^R$ complex, namely, area of contact, dissociation constant, spacial arrangement and interaction strength of nonbonded residues, water population, and heme-heme distance in terms of a distribution, and not just a single numerical value.

MD simulation enhances binding interface contact

In the case of pre-ET $(c_2^O c_1^R)$ state, the contact area of the cyt. c_2 - cyt. c_1 interface increased from 956 Å^2 to 1256 Å^2 over the first 5 – 10 ns of MD simulation, after which time the area typically stabilized at this mean value, fluctuating with deviations of ±198 Å^2 (Fig. 2b). A similar increase in contact area relative to the initial structure was reported in MD simulations of yeast cyt. c - cyt. c_1, in which case the area increased from 880 to 1247–1555 Å^2 in 3 – 5 ns.[19] An increase in binding contact area during initial MD equilibration indicates a relaxation of the complementary binding partners at the interface (Fig. 2c), as well as an onset of dynamic interactions that are not captured by a stationary docked model. As discussed below, dynamic adhesion, which is not accounted for in the initial docked model, adds not only to the predicted binding strength of the cyt. c_2 - bc_1 complex, but reveals also a significant correlation between the motion of cyt. c_2 and of the iron-sulfur protein. Regardless, for now it is noted that the MD simulated cyt. c_2 - bc_1 complex contact area of 1256±198 Å^2 in *Rba. sphaeroides* is in good agreement with its yeast counterpart (1381±163 Å^2).[19]

Electrostatic and hydrophobic interactions stabilize the binding interfaces of $c_2^O c_1^R, c_2^O c_1^O, c_2^R c_1^R$, and $c_2^R c_1^O$

A list of interactions stabilizing the cyt. c_2 - cyt. c_1 interface is provided in Table 1 and Table S3. The presented interactions have been determined from MD simulations of four redox states of the cyt. c_2 - cyt. c_1 complex, namely $c_2^O c_1^R$ (pre-ET), $c_2^O c_1^O, c_2^R c_1^R$, and $c_2^R c_1^O$ (post-ET) (see Table S1).

To identify the interface stabilizing interactions, we consider the MD simulation of the pre-ET state first, as this is, functionally speaking, the initial state when an oxidized cyt. c_2 approaches a bc_1 complex with a reduced cyt. c_1. This state permits electron transfer from bc_1 complex to cyt. c_2 and is, thus, most relevant for cyt. c_2 - cyt. c_1 docking.

The cyt. c_2 - cyt. c_1 docking surfaces of the energetically most favorable pre-ET complex are illustrated and characterized in Fig. 2a. The surfaces exhibit a clear complementarity, namely a half-ring peripheral arrangement of oppositely charged residues that enclose polar and hydrophobic residues within a tight core; it is noteworthy that the cyt. c_2 and cyt. c_1 heme groups are encased within these hydrophobic cores. The adhesion interactions can be classified into long-range electrostatic, medium-range charge-polar and polar-polar, and short-range van der Waals interactions. In addition, our simulations suggest the presence of cation-π interactions at the docking interface.

The long-range interactions between basic residues of the cyt. c_2 half-ring (residues R32, K35, K55, K95, K97, K99, K103, and K105) and complementary acidic side chains of the cyt. c_1 half-ring (residue E141, E147, E150, D152, D80, E95, and E34) are seen in the MD simulation to exhibit more dynamic adjustment than the amino acids involved in intermediate or short-range interactions. Listed in Table S3, distances between the complementary charged residues exhibit a significantly larger variance than those of the hydrophobic residues. The simulation reveals also that water molecules at the cyt. c_2 - cyt. c_1 interface mediate a majority of the electrostatic interactions, thus, rendering these interactions dynamic. One can notice that these dynamical electrostatic interactions remain strong even at cyt. c_2 distances of 10–12 Å from the bc_1 complex surface and, thereby, achieve long-distance recognition of the half ring patterns for cyt. c_2 binding. In contrast to the charged residues, the polar and the hydrophobic residues (residue T17, T101, F102 of cyt. c_2 and A38, M190, L193 of cyt. c_1) avoid water, are tightly packed via short-range interactions and, thereby, exhibit reduced fluctuations. The role of water molecules mediating interfacial electrostatics will be elaborated further in Discussion.

Short-range interactions between the hydrophobic residues of cyt. c_2 and cyt. c_1 in the immediate neighborhood of their heme groups allow the two hemes to get into close proximity of each other. As listed in Table S4, the edge-to-edge distance between the two hemes derived from MD simulation of the pre-ET complex is 8.48 ± 0.21 Å, which is in good agreement with the distance of 9.1 Å seen in the yeast crystal structure of the cyt. c_2 - bc_1 complex.[14] The distance of closest approach between carbon atoms of the cyt. c_2 and cyt. c_1 hemes is found in our simulation to be 4.06 ± 0.76 Å (Fig. 3a); both distances discussed here are marginally larger for the post-ET state $(c_2^R c_1^O)$. The short inter-heme spacing is too small to allow water between the heme edges and permits direct heme-to-heme electron transfer from bc_1 complex to cyt. c_2.[46] Such direct transfer path is in sharp contrast to amino acid-mediated electron transfer suggested for the cyt. c_2 - RC complex.[47,48] A distribution of heme-heme geometries is observed in Fig. 1b indicating clearly that for comparable edge-to-edge distances there exists an ensemble of multiple protein and heme conformations each of which are perfectly capable of direct electron transfer.

Another striking feature of the adhesion between cyt. c_2 and cyt. c_1 that all the four MD simulations (Table S1) reveal is a mobility-mismatch between the complementary charged residues. As illustrated in Fig. 3a–b, positive residues on the surface of cyt. c_2 exhibit larger positional variance and, thereby, a fuzzier conformational distribution than the negative ones contributed by cyt. c_1. As a result, the cyt. c_1 surface is found to accommodate a substantial number of structured water molecules at the interface, as has also been observed crystallographically for yeast cyt. c_1 (Fig. 3a inset).[10] The mobility mismatch, due to binding-induced changes in the stability of cyt. c_2 and cyt. c_1 docking faces, is discussed further below.

All the four MD simulations indicate further a cation-π interaction between residues K35 of cyt. c_2 and F154 of cyt. c_1, consistent with crystallographic findings in yeast.[10] However, given the limitations of available force fields in accurately capturing such interactions, the energies are underestimated typically by a factor of two relative to values calculated from density functional theory for an isolated cation-π bond.[49] The values calculated here, even though underestimated, can still be qualitatively reconciled with existing knowledge on the role of cation-π interactions at the cyt. c_2 - cyt. c_1 interface, because, (a) isolated cation-π interactions are not the best estimate of their contribution in a real protein-protein interface and, (b) indeed, calorimetric experiments have revealed considerably weaker cation-π interactions of ~1 kcal/mol at the cyt. c_2 - RC interface, indicating the lability of these interactions.[20] Therefore, as argued in Section S2 of SI, it seems advisable to defer discussion of the role of cation-π interactions for docking cyt. c_2 to the bc_1 complex until further quantitative experimental data are available.

Finally, we note in Section S3 of SI some of the interface stabilizing residues on the bc_1 complex that are identified during the MD simulation of the pre-ET state, such as E141, E34, D191, D192, and D152. These residues remain conserved in other photosynthetic and respiratory life forms including *Rba. capsulatus*, *Chlamydomonas reinhardtii* and *Bos taurus*.[24] Such evolutionary evidence further supports the interaction analysis of Table 1 in demonstrating the essential role of interface-binding residues predicted from our docking analysis and MD simulations.

Redox state control of interfacial interactions

Conformational changes at the cyt. c_2 - cyt. c_1 docking interface were further analyzed on the basis of the MD simulations (Table S1) of the four possible redox states of the complex, namely $c_2^O c_1^R$ (pre-ET), $c_2^O c_1^O$, $c_2^R c_1^R$, and $c_2^R c_1^O$ (post-ET). As suggested by the interaction energy data in Tables 1, S3, and illustrated in Fig. 4a, changes to cyt. c_2 - cyt. c_1 adhesion in the pre-ET state result from cyt. $c_1 \rightarrow$ cyt. c_2 electron transfer, due to changes of the electrostatic interactions between cyt. c_2 and the bc_1 complex. The electrostatic interactions are seen to decrease in going from $c_2^O c_1^R$ to $c_2^R c_1^O$. Coincidentally, the first three redox states, $c_2^O c_1^R$, $c_2^O c_1^O$ and $c_2^R c_1^R$, have been crystallographically isolated for yeast,[10] confirming their higher stability relative to the fourth, post-ET state, $c_2^R c_1^O$, which, indeed, should be functionally unstable as cyt. c_2 needs to separate from the bc_1 complex after electron transfer. Consistent with the decrease in interfacial adhesion, the contact area, as seen in our

simulations, strongly decreases from the pre- to the post-ET states (Fig. 2b inset). Structural details underlying the weakness of cyt. c_2 - cyt. c_1 binding (Table S3) after electron transfer from cyt. c_1 to cyt. c_2 are further examined in Discussion.

Note, $c_2^O c_1^O$ represents a state where the oxidized cyt. c_2 has arrived at the bc_1 complex surface, but the electron from quinol is yet to be transferred into the cyt. c_1 - heme. The cyt. c_1 surface in $c_2^O c_1^O$ is therefore less negatively charged than that in $c_2^O c_1^R$. Consequently, the cyt. c_2 - cyt. c_1 binding interactions in $c_2^O c_1^O$ are weaker than in those $c_2^O c_1^R$. Nonetheless, these interactions are still higher than those in $c_2^R c_1^R$ and $c_2^R c_1^O$, and sustains an adhesive cyt. c_2 - cyt. c_1 interface prior to the arrival of the electron at the cyt. c_1 - heme. Thus, formation of the $c_2^O c_1^O$ complex supports a cyt. $c_1 \rightarrow$ cyt. c_2 electron transfer within the photosynthetic energy conversion scheme of Fig. S3. In contrast, $c_2^R c_1^R$ represents a state, where following electron transfer and unbinding from the oxidized bc_1 complex, the reduced cyt. c_2 binds to a second reduced bc_1 complex instead of reaching the electron deficient RC protein. This mis-targeted state does not support the cyt. $c_1 \rightarrow$ cyt. c_2 electron transfer and is expected to reduce the photosynthetic energy conversion efficiency of the scheme in Fig. S3. Our computations reveal that the electrostatic interactions in $c_2^R c_1^R$, though adhesive, are one of the weakest of the four redox states, undermining thereby, the *in vitro* feasibility of this complex. A comparison of cyt. c_2 - cyt. c_1 interactions in $c_2^R c_1^R$ (Table S2), with the cyt. c_2 - RC interactions from ref.,[27] together with data from steady state kinetics studies,[11,50,51] further demonstrates that formation of the former complex is less thermodynamically favorable. Thus, the population of the $c_2^R c_1^R$ complex is naturally screened during the photosynthetic energy conversion cycle by formation of the more functionally relevant c_2^R - RC complex.

Three key observations pertaining to the unbinding of cyt. c_2 from the bc_1 complex are made from the MD simulations. (i) The decrease in adhesion between cyt. c_2 and bc_1 complex in going from the pre- to the post-ET states was seen to be accompanied by an enhancement of cyt. c_2 and cyt. c_1 surface fluctuations (Fig. 3c) yielding, thus, even fuzzier interface conformations than those of Fig. 1b (Fig. 4c). (ii) The cyt. c_2 fluctuations remain consistently higher than those of cyt. c_1 in all four redox states, thus, maintaining a mobility-mismatch both before and after the electron transfer. In the post-ET complex, which is prone to unbinding, both cyt. c_2 and cyt. c_1 surfaces are found to exhibit maximum surface fluctuations and still the highest mismatch (Fig. 3c). (iii) The loss of interfacial adhesion of the post-ET complex is followed by an increase in the number of water molecules at the binding interface (Fig. 4b). Pronounced surface fluctuation in this complex lowers the density of structured water at the interface (Fig. 4b inset vs. Fig. 3a), further adding to interface mobility and, thereby, inducing dissociation of the complex. In fact, as discussed in Section S4, the interfacial water undergoes an order-disorder transition from a structured to an unstructured state in going from the pre- to the post-ET states.

The variation in interface interaction energies, in response to changes in the heme redox states of cyt. c_2 and cyt. c_1, strongly depends on the partial charge of the complementary binding partners. One can see from Table 1c that the short-range van der Waals interactions

due to hydrophobic residues vary only marginally with electron transfer; this variation is in contrast to the variations seen in the long-range electrostatic interactions that are due to charged residues and heme groups and, actually, give rise to large energy difference between four possible redox states. Illustrated in Fig. S2, the hydrophobic residues encasing the heme groups are similarly oriented before and after the inter-heme electron transfer, i.e., in states $c_2^O c_1^R$ and $c_2^R c_1^O$. This independence of the short-range interactions on the redox state has also been observed in three cyt. c - cyt. c_1 complexes for yeast (PDBID: 1KYO, 3CX5, and 1YEA). In these systems, the hydrophobic groups in the immediate neighborhood of the heme moieties constitute a "minimal core" of short-range interactions that permits the close heme-heme spacing necessary for direct electron transfer.[10] The feasibility of the close hydrophobic minimal core described is now demonstrated for all four possible redox states of the *Rba. sphaeroides* cyt. c_2 - bc_1 complex.

Steered MD simulations reveal pathways of cyt. c_2 binding/unbinding

Ten independent 50-ns SMD simulations for the two key redox states (listed in Table S1) revealed similarities and differences in the unbinding of the cyt. c_2 - bc_1 complex in its pre- and post-ET states. Under the assumption of microscopic reversibility, the unbinding of cyt. c_2 sheds light also on the pathway(s) of binding.

The results of our unbinding simulations shown in Fig. 5 are consistent with the equilibrium simulation results shown in Fig. 4a and Table 1a; the majority of the long-range electrostatic interactions are attractive in the pre-ET state, covered in Fig. 5a, and, indeed, these interactions together with the van der Waals interactions are seen to cohesively stabilize the binding interface for the first 15 ns of steering that attempts to pull the complex apart. In the post-ET state (Fig. 5b), the long-range interactions are relatively weak, and only the short-range van der Waals contacts contribute to interface adhesion, holding the complex together for 15 ns despite the application of pulling forces. In fact, the simulations clearly show that complementary charged, polar and hydrophobic residues remain strongly correlated across the $c_2^O c_1^R$ interface (Fig. S4a in SI); only the polar and hydrophobic residues retain such correlation after electron transfer (Fig. S4b), further confirming the loss of electrostatic interactions after electron transfer. The detailed correlation patterns are derived employing the dynamical network analysis[52] of VMD.[38]

Nonequilibrium work profiles derived from the SMD simulations of the pre- and post-ET complexes, presented in Fig. S5 and presented in Section S5, are consistent with the energy changes shown in Fig. 5, demonstrating that the initial phase of unbinding involves mainly work to overcome strong van der Waals and/or electrostatic interactions; this work subsides later on in the trajectory. As detailed in Section S6, unbinding of cyt. c from the bc_1 complex in yeast follows a similar work profile, suggesting a binding/unbinding pathway comparable to that of *Rba. sphaeroides*. Given that the cyt. c-bound bc_1 complex is found across a broad range of eukaryotes, its agreement with the binding/unbinding pathways derived from our computationally docked model of cyt. c_2 -bound bc_1 complex argues for the biological relevance of the present findings.

Finally we note three key observations, labeled below (i), (ii) and (iii), made during the SMD simulations that directly relate to the regulation of the bc_1 complex binding/unbinding of cyt. c_2, and cyt. $c_1 \rightarrow$ cyt. c_2 through the electron transfer process. (i) When steering apart cyt. c_2 in the $c_2^O c_1^R$ complex, first, an intermediate scale electrostatic interaction between K99 and E95, which is among the weakest charge-charge interactions listed in Table 1a, is lost (Fig. 5a inset). The van der Waals contact disrupts after 10 ns and, finally, the remaining long-range electrostatic interactions, which are stronger than the van der Waals interactions, unbind after 15 ns. In Discussion we examine further how this trade-off between long- and short-range interactions accompanies electron transfer.

(ii) Independent SMD simulations, performed with the same steering protocol, proceeded via multiple equally likely pathways that are characterized by similar energy profiles, but differ by the sequence of unbinding between the electrostatic pairs (Fig. S8). Assuming microscopic reversibility, the involvement of multiple unbinding pathways suggests the existence of multiple binding pathways of cyt. c_2; each pathway is equally favorable, but is mediated by a different sequence of binding between the charged residues. The conclusion is in line with EPR measurements that likewise suggest the existence of a cloud of multiple equally bindable cyt. c_2 domains in the vicinity of a reduced cyt. c_1 surface.[17]

(iii) The minimal core that encases the heme groups is not necessarily limited to the perfectly docked cyt. c_2 conformation(s); rather, the relevant hydrophobic residues begin to interact already when the hemes of cyt. c_2 and cyt. c_1 are 12–13 Å apart (Fig. S6). Furthermore, unlike equilibrium configurations where minimal core interactions are nearly redox-independent (see Table 1c), in the SMD simulations minimal core contacts in $c_2^R c_1^O$ are found to be consistently more separated than those in $c_2^O c_1^R$ (Fig. S7), a characteristic that $c_2^R c_1^O$ leverages to avoid reverse electron transfer from the reduced cyt. c_2 back to bc_1 complex.

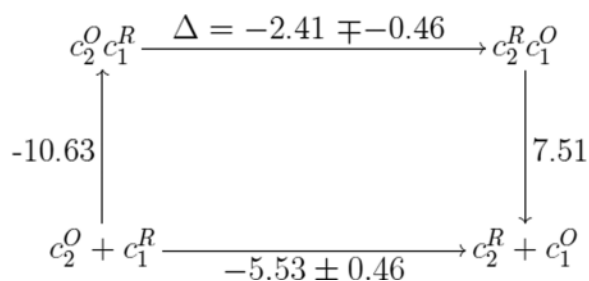### Thermodynamics of cyt. c_2 binding/unbinding

Dissociation constant (K_d) and binding free energy of the MD simulated structures of the pre- and post-ET complexes were computed using a bioinformatics-oriented approach on the CRYSTAL STRUCTURE K_d SERVER from the SEQMOL suite (biochemlabsolutions.com). The software employs scoring functions involving experimentally determined binding parameters, accumulated over hundreds of complexes reported in the PDB, and the input structure to measure the binding free energy and interface dissociation constant. Fifty structures, saved every ns over the final 50 ns of MD trajectories involving the pre- and post-ET complexes, were separately processed on the server to compute the corresponding K_d. The average K_d of the pre- and post-ET complexes were found to be 0.03 μM and 0.11 μM respectively, in excellent agreement with 0.06 μM and 0.22 μM obtained from plasmon waveguide resonance spectroscopy experiments of the cyt. c_2 - cyt. c_1 complex.[53] Recovery of such realistic K_d values for the cyt. c_2 bound bc_1 complex of *Rba. sphaeroides* further reinforces confidence in the docked model presented here.

Note, the experimentally determined K_d values for the post-ET complexes range from 0.11 μM up to 3.4 μM.[53] The MD simulations have converged to a relatively tightly bound state of these complexes that exhibit smaller K_d values; the more weakly bound, 3.4 μM, complexes remain obscure to the MD simulations. Determination of only the tight post-ET complexes is expected due to the limited timescale (150 ns) of the MD simulations. Within this timescale the simulated post-ET complex relaxes into a state which is indeed less stable than the pre-ET complex and, thus, prone to cyt. c_2 unbinding (Fig. 4a); however, this state fails to capture the much weaker cyt. c_2 - cyt. c_1 interactions of the 3.4 μM complexes that is absolutely necessary to unbind cyt. c_2. Unlike MD, such weak interactions are captured in the SMD simulations (Fig. 5c: 50 ns), which indeed features complexes with computed K_d values in the range of 3.1 – 3.4 μM; these complexes are collected over the final 5 ns of each of the five 50-ns SMD simulations.

The simulated and observed K_d values together with the known redox potentials cyt. c_2 - bc_1 complex contain information on the binding and redox energetics of this redox partner system. This system can be described through four states, namely $c_2^O c_1^R$ and $c_2^R c_1^O$, defined above, and $c_2^O + c_1^R$, and $c_2^R + c_1^O$, which correspond to the same redox states, but for separated cyt. c_2 and bc_1 complex. The four states form a thermodynamic cycle presented along with the respective energy values, in units of kcal/mol, in Scheme (1). If one defines the energy of redox state $c_2^O + c_1^R$ as the (zero) reference energy, then the energy of redox state $c_2^R + c_1^O$ is in the range −5.07 to −5.99 kcal/mol (see lower arm of Scheme (1)). This range of values is deduced from the well-known redox potential energy differences of −220 to −260 mV for the reaction $c_2^O + c_1^R \rightarrow c_2^R + c_1^O$ between cyt. c_2 and its typical single-electron redox partners like the bc_1 complex.[54] The energy of state $c_2^O c_1^R$ is calculated from the association reaction $c_2^O + c_1^R \rightarrow c_2^O c_1^R$ to be −10.63 kcal/mol. Labeled on the left arm of Scheme (1), the latter energy is computed employing the relationship $E = RT \ln(K_d)$, where K_d for $c_2^O + c_1^R \rightarrow c_2^O c_1^R$ is 0.03 μM. If one assigned to $c_2^O c_1^R \rightarrow c_2^R c_1^O$ electron transfer (labeled on the upper arm of Scheme (1)) an energy , then the energy of state $c_2^R c_1^O$ is −10.63 kcal/mol + . Finally, the energy difference between states $c_2^R c_1^O$ and $c_2^R + c_1^O$ (labeled on the right arm of Scheme (1)) is given by the K_d value of 3.4 μM[53] for the $c_2^R c_1^O \rightarrow c_2^R + c_1^O$ disociation reaction; the numerical value translates into an energy of $E = RT \ln(K_d) = 7.51$ kcal/mol. Note, even though our MD simulation has delivered $c_2^R c_1^O$ complexes with K_d values of ~0.11 μM, majority of the post-ET population is characterized by 3-fold weaker $c_2^R c_1^O$ complexes with K_d values of ~3.4 μM,[53] which is also captured in SMD. Consequently, dissociation energy of the weaker complexes is considered for computing the energetics of electron transfer.

The thermodynamic cycle characteristics summarized above and in Scheme (1) lead to an interesting implication about the biological design of the cyt. c_2 - bc_1 complex redox partner system. Clearly, $c_2^O + c_1^R \rightarrow c_2^R + c_1^O$ electron transfer is energetically favorable by −5.5 ± 0.45 kcal/mol. According to the thermodynamic cycle the binding, electron transfer and unbinding steps consuming an energy of −10.63 kcal/mol + + 7.51 kcal/mol should add up to the redox energy −5.53 ± 0.46 kcal/mol. This implies for small values in the range of

−2.41 ± 0.46 kcal/mol. One can conclude from the thermodynamic cycle then an important, amazingly optimal, strategy of the cyt. c_2 - bc_1 complex system, namely to invest almost 60 % of the negative (−5.53 ± 0.46 kcal/mol) energy into recognition and binding of the partners, rather than electron transfer. Clearly, the underlying strategy to use redox energy for partner recognition and binding is optimal for the cell, in particular, as the role of cyt. c_2 in cellular bioenergetics is often rate limiting.[9,10]

$$c_2^O c_1^R \xrightarrow{\ \Delta = -2.41 \mp -0.46\ } c_2^R c_1^O$$

$$\Big\uparrow -10.63 \qquad\qquad\qquad 7.51 \Big\downarrow$$

$$c_2^O + c_1^R \xrightarrow{\ -5.53 \pm 0.46\ } c_2^R + c_1^O$$

(1)

Summarizing the key results, in agreement with prior experiments our simulated model of the cyt. c_2 bound bc_1 complex reveals dynamic electrostatic interactions, a tightly packed hydrophobic minimal core, close inter-heme distances and mobility mismatch at the binding interface. We have also now established that the strong influence of the electrostatic and hydrophobic interactions is not limited to the docked state; rather these interactions play a major role in interface recognition when both the cyt. c_2 and bc_1 complex are out of their docked conformations. The cyt. c_2 binding is highly targeted, driven by a half-ring pattern of complementary charged residues on the bc_1 complex surface, yet multiple equally-likely bc_1 complex approach pathways exist for cyt. c_2. Consequently, there is no single bound state, but an ensemble of bound states characterized by μM-scale dissociation constants and satisfying the crystallographically determined structural features. Lastly, we discovered that electron transfer from cyt. $c_1 \rightarrow$ cyt. c_2 disrupts interfacial electrostatic interactions and enhances interface mobility to ultimately induce the unbinding of cyt. c_2.

Discussion

In this section, functional and mechanistic inferences are drawn from the above results of this study. First, we discuss the role of long-range electrostatic interactions in mediating cyt. c_2 recognition and binding to the bc_1 complex. Second, changes in the conformation and mobility of charged residues at the interface in response to cyt. $c_1 \rightarrow$ cyt. c_2 electron transfer are discussed to elucidate how dynamics at the side group level induce interface-wide events, such as cyt. c_2 unbinding. Third, it is explained how electron transfer is promoted by hydrophobic interactions between the non-polar residues at the interface. Fourth, dynamical correlation between cyt. c_2 and the ISP is explored to discuss the direct role of cyt. c_2 unbinding in quinol oxidation. Finally, discussions across the above four facets are tied into a logical order to provide a detailed picture of cyt. c_2 recognition, binding and unbinding mechanism. This mechanism portrays how the architecture of cyt. c_2 is

leveraged in photosynthetic and respiratory pathways to enable timely single-electron transport between the integral membrane proteins.

Well-defined, dynamic cyt. c_2 docking surface

As illustrated in Fig. 2, the electrostatic interactions at the cyt. c_2 - cyt. c_1 interface stem from residues that form complementary half-rings surrounding in each partner weakly polar and non-polar residues. Five oppositely charged interaction pairs are identified in the half-rings (Table 1a). The interaction pairs include contributions from amino acids K95 to K106 in cyt. c_2, which have been shown by single-point mutation experiments to be key for the binding of cyt. c_2 to the bc_1 complex in *Rba. sphaeroides*;[13] dipolar interactions involving Y155, reported in Table 1b, have also been demonstrated to be critical in stabilizing the cyt. c_2 - bc_1 complex interface in *Rba. capsulatus*.[25]

A half-ring peripheral arrangement of the interacting partners orients their electric dipoles to a definite azimuthal direction that provides the basis for a well-defined docked state. In contrast, a circular arrangement could have invoked rotationally equivalent and equally feasible binding patterns, thus likely involving heme - heme geometries not suitable for direct electron transfer.[46] Besides, undocking of a circular arrangement, rather than a half-ring arrangement, would be energetically more demanding and slow, which might ultimately reduce the overall rate of ATP synthesis as the cyt. c_2 - bc_1 complex redox reaction is likely rate limiting.[55] Furthermore, the half-ring arrangement of charged residues is a common feature among the three electron transfer complexes cyt. c - bc_1 complex, cyt. c_2 - reaction center, and cyt. c - cyt. c peroxidase.[21,22] Thus, the predicted half-ring arrangement of complementary residues, which clearly defines an orderly docking geometry, is expected to be optimal for efficient electron transfer from bc_1 complex to cyt. c_2.[56,57]

The electrostatically interacting residues are separated across the docking partners by distances of 7 – 12 Å (Table S3). These distances are comparable to the Debye length of 9.6 Å between single-charged ions at an ionic concentration of 100 mM.[58] The distance values suggest the absence of direct salt-bridge interactions between the binding faces of cyt. c_2 and cyt. c_1. Rather, 1.5 times more interfacial water than found on typical protein-protein interfaces[14] renders the water-mediated electrostatic interactions highly dynamic and, thus, cyt. c_2 - bc_1 complex interface conformationally fuzzy. The dynamics of the interface exhibits conformational freedom described by an ensemble of docked cyt. c_2 states (Fig. 1b), all of which allow fast enough electron transfer due to the constraints imposed by the overall half-ring binding pattern and close inter-heme geometries.

Interestingly, water molecules associated with the cyt. c_2 side of the interface are less structured than those with the cyt. c_1 side. As shown in Figs. 3, 4, the absence of structured water in the vicinity of the cyt. c_2 binding surface coincides with a higher mobility of the associated positively charged side chains relative to those of the negative cyt. c_1 residues, thereby, resulting in a mobility-mismatch.

Role of mobility mismatch

In order to investigate the role of the mobility mismatch at the cyt. c_2 - bc_1 complex interface we also carried out an MD simulation of an isolated cyt. c_2 to compare the dynamics of its

binding surface residues in the docked and undocked states. The new simulation suggests that the positive cyt. c_2 residues R32, K35, K55, K95, K97, K99, K103, and K105, which are the electrostatic partners to cyt. c_1 in the docked case, in the undocked case form strong intra-cyt. c_2 salt bridges with residues D52, E59, D82 and D93. Upon binding of cyt. c_2 to the bc_1 complex, the intra-cyt. c_2 salt bridges are replaced by weaker, water mediated, long-range electrostatic interactions with cyt. c_1 residues E141, E147, E150, E152, D80, E95, and E34 (see Table 1). Consequently, cyt. c_2 marginally loses stability after binding to the bc_1 complex (Figs. S11a and S10) and its surface residues become more mobile (Fig. 3a).

Unlike undocked cyt. c_2, undocked cyt. c_1 lacks any substantial internal interaction partners for its surface glutamate and aspartate residues. Thus, cyt. c_1, upon binding to cyt. c_2, gains complementary partners and, thereby, stability (Figs. S11b and S10), as well as decreased surface mobility, explaining the mobility mismatch at the cyt. c_2 surface. Subsequently, negatively charged cyt. c_1 residues and positively charged cyt. c_2 residues orient the dipole moments of the interfacial water molecules (Fig. S12a), with the water-hydrogens pointing towards the bc_1 complex surface, promoting hydrogen bond formation between water molecules and the negatively charged residues at the surface. As a result, the hydrogen-bonded water molecules on the bc_1 complex surface are found ordered and, therefore, less mobile relative to those in the vicinity of cyt. c_2.

The predicted decrease in thermal stability of cyt. c_2 upon binding to the bc_1 complex, employed here to rationalize the mobility mismatch, is independently supported by microcalorimetric experiments that show the denaturation temperatures of cyt. c to decrease after binding.[59] Taken together, our explanation of the mobility mismatch rationalizes crystallographic findings on the surface water accessibility[10] with the thermodynamics of binding interface stability, linking two seemingly exclusive experiments.

Finally, the mismatch in mobility of residues at the cyt. c_2 and cyt. c_1 binding surfaces reflects a key structural element that cyt. c_2 employs to redox-selectively bind as well as unbind the bc_1 complex. A low extent of mismatch before the electron transfer from cyt. c_1 to cyt. c_2, shown in Fig. 3c, ensures a μM-scale dissociation constant of the $c_2^R c_1^O$ complex; this medium-range protein-protein dissociation constant[60] suffices, on the one hand, for adhesive cyt. c_2 binding, and on the other hand, facilitates a bc_1 complex residence time of ~11 ms, supporting the overall 25 ms turnover time for cyt. c_2.[8] The ensuing electron transfer is followed by an increase in mobility mismatch at the interface and a 3–10 fold decrease of the dissociation constant which facilitates, in turn, the unbinding of cyt. c_2. Conversely, if the mobility mismatch were absent, two situations would have arisen, but neither being sufficient to maintain the optimal rate of cyt. c_2 turnover: first, if both surfaces were equally highly mobile and, therefore, unstable after binding, cyt. c_2 would have always avoided cyt. c_1 binding and subsequent electron transfer; second, if both surfaces became less mobile and, therefore, stabilized after binding, the mobile, water mediated, cyt. c_2 - bc_1 complex electrostatic interactions would be replaced by direct salt bridges. Purely for dielectric reasons these salt bridges would be 10-fold stronger than water-mediated interactions[27] making the bc_1 complex residence time of cyt. c_2 at least e^{10}-fold longer and, thus, disrupting the overall efficiency of cyt. c_2 turnover.

Cyt. c_2 unbinding via a redox-dependent lysine-switch

The results of our simulations show that the electrostatic interaction between cyt. c_2 and bc_1 complex decreases along the redox states $c_2^O c_1^R$ to $c_2^O c_1^O$ to $c_2^R c_1^R$ to $c_2^R c_1^O$ (Table 1a). Consequently, the area of contact between cyt. c_2 and cyt. c_1 follows a similar trend (Fig. 2). Here, we discuss how atomic-scale conformational changes in response to variations in the cyt. c_2 or cyt. c_1 heme oxidation states affect the electrostatic interaction across the binding interface.

The electrostatic interactions listed in Table 1a, for the most stable bound redox state, $c_2^O c_1^R$, range from −25 to −10 kcal/mol. The interaction between K99 of cyt. c_2 and E95 of cyt. c_1, though significant, is one of the weakest interface-stabilizing electrostatic interactions. Therefore, on external perturbation, this interaction is expected to be more readily weakened than the other, stronger, interactions (Fig. 5a inset). In fact, such a perturbation to the $c_2^O c_1^R$ bound state occurs when the electron is transferred from the bc_1 complex to cyt. c_2, generating the $c_2^R c_1^O$ state, in which the potential on the cyt. c_2 heme region becomes more negative (Fig. 6b inset). As a result, the E95-bound K99 lysine becomes attracted towards the carboxylate group of the cyt. c_2 heme (Fig. 6b) and switches its salt bridge from E95, stable in the $c_2^O c_1^R$ state (Fig. 6a), to a cyt. c_2 heme carboxylate in the $c_2^R c_1^O$ state (Fig. 6b). Weakening of the K99-E95 interaction opens space for water to intrude into the interface, thereby, facilitating cyt. c_2 unbinding (Fig. 4a) through increased fluctuations of the surface residues and the resulting destabilization of the binding interface. The statistical significance of the lysine-switch is established by counting the time intervals in which the K99-E95 bond is formed in the fuzzy pre-ET complex and the time intervals in which a K99-heme carboxylate bond is formed in the post-ET complex (Fig. S14).

The switching of lysine is supported by crystal structures that show a strong conformational change in the lysine equivalent to K99 between oxidized and reduced states of yeast cyt. c_2 (namely, K84 in 1YKO and 3CX5, and K79 in 1YEA; see Fig. 6). Electrochemical studies of cyt. c in yeast[62] further suggest that the lysine(K79)-switch interactions exclude some excess water from the binding interface to bring the bc_1 heme closer for a direct electron transfer. A lysine-switch is seen, in MD simulations, to also play a role in stabilizing the cyt. c_2 - RC interface.[27]

Altogether, the decrease in cyt. c_2 - cyt. c_1 interface stability from pre- to post-ET redox state is explained mainly on the basis of the extent of lysine-switching. Summarized in Table S3, lysine-switching happens the least before the electron transfer, in $c_2^O c_1^R$ and $c_2^O c_1^O$, where the K99-E95 bond is present, keeping the interface relatively stable. The extent of switching increases after the electron transfer, in $c_2^R c_1^R$ and $c_2^R c_1^O$, where the K99-E95 bond is replaced by the K99-heme carboxyl interaction and where all the dominant interfacial electrostatic interactions are attenuated.

In addition to inducing unbinding of cyt. c_2, the lysine-switch can be viewed as a heme redox recognition element. Only an oxidized cyt. c_2 with K99 not interacting with the heme will be able to interact with E95 residue of cyt. c_1 forming $c_2^O c_1^R$ and $c_2^O c_1^O$ complexes. In

contrast, a heme-carbonyl bound K99 as it exists in reduced cyt. c_2, will find it difficult to interact with the E95 of cyt. c_1, therefore naturally reducing the population of complexes $c_2^R c_1^R$ and $c_2^R c_1^O$.

Role of minimal core for heme-heme electron transfer

Inter-protein electron transfer has been investigated previously in case of a cyt. c_2 - RC encounter pair.[14,27] A key difference between the cyt. c_2 - RC complex and the cyt. c_2 - bc_1 complex is the electron transfer distance. In the former, an edge-to-edge distance for electron transfer of 14 Å is reached in the docked state;[16] in the latter, however, the edge-to-edge distance in the docked state is 9 Å, the shorter distance brought about by the so-called minimal core. Since fast physiological electron transfer is observed for edge-edge distances of up to 14 Å,[46] in principle, electron transfer in case of the cyt. c_2 - bc_1 complex could already occur while cyt. c_2 is approaching its fully docked state. One may then ask whether the bc_1 complex forms multiple productive complexes with cyt. c_2 with inter-heme distances of > 9 Å or whether a mechanism exists that prevents less efficient complexes and favors formation of a narrowly defined single complex. Our simulations addressed the questions as follows.

SMD simulations of the pre-ET complex, $c_2^O c_1^R$, show that the hydrophobic minimal core which encases the heme groups, can remain intact for the first 10 ns of steering when interheme distance increases from 10 to 12–13 Å (Fig. S6). Consequently, it is possible that electron transfer is still mediated via the minimal core even if the cyt. c_2 heme is out of its equilibrium conformation; also, the dissociation constant of the cyt. c_2 - bc_1 complex in the pre-ET state remains between 0.03 μM and 0.06 μM (close to experimental numbers) when the inter-heme distance is increased up to 13 Å. The minimal core itself is rigid and forms only after half-ring oriented electrostatic interactions get cyt. c_2 close to the bc_1 complex, ensuring orientational restriction between the heme moieties. Thus, it seems that electron transfer can occur only for an ensemble of docked states that exhibit a well-defined minimal core which keeps the hemes within proximity and orientation. However, multiple binding pathways in regard to direction of approach or to binding sequence (see Fig. S8) are permitted such that a rather broad docking funnel can guide the system to a heme-heme conformation suitable for efficient electron transfer.

Inferences on binding/unbinding mechanisms

The results of our MD and SMD simulations provide a model for bc_1 complex recognition, binding, and unbinding of cyt. c_2 in *Rba. sphaeroides*. First, long-range electrostatic interactions, between an oxidized cyt. c_2 and a reduced bc_1 complex, allow for recognition of complementary half-ring binding patterns to yield an encounter complex. The formation of this complex is followed by establishing the intermediate scale charge-charge and charge-polar interactions and, subsequently, the short-range van der Waals, minimal core interactions when the docking partners approach each other within 5–7 Å. Finally, the lysine switch is formed signaling the last binding step. The close inter-heme distance permitted by the fuzzy docked conformations allows for rapid electron transfer to take place. After the electron transfer, the lysine switch breaks and interface mobility mismatch sets in, thereby

weakening the electrostatic interactions at the interface through hydration. The surfaces, now water-exposed, force the hydrophobic residues to bury themselves within the surfaces of their respective proteins to avoid solvent, thus loosening the interface hydrophobic contact. This loosening of the hydrophobic contacts facilitates further separation of the two hemes, thus, reducing the probability of a reverse electron transfer. Finally, the already weakened long-range electrostatic interactions are screened away by the growing water population at the interface, causing cyt. c_2 to unbind from the bc_1 complex. Described in Section S7 of the SI, the iron-sulfur protein then unbinds from cyt. c_1 to return towards the quinol binding site where it acquires a new electron to replenish the oxidized cyt. c_1 in the next cycle.

Conclusions

The present study establishes a first all-atom model of cyt. c_2 recognition, binding, and unbinding of the bc_1 complex in *Rba. sphaeroides*. The model is further shown to be applicable for the more ubiquitous cyt. c - bound bc_1 complexes. In particular, we show how single-electron transport complexes tune their non-bonded (electrostatic and van der Waals) interactions to recognize and respond to the different stages of electron transfer. Addressing these interactions provides direct structural and functional insights into key rate-determining bioenergetic processes that underlie photosynthesis and respiration. We find: (i) a non-degenerate half-ring binding pattern of the cyt. c_2 molecule on the bc_1 complex primarily guided through electrostatic interactions that enable long-range recognition and optimal orientation; (ii) the structure and physical characteristics of a hydrophobic core which allows close inter-heme proximity and direct bc_1 complex to cyt. c_2 electron transfer; (iii) a distribution of conformations characterizing cyt. c_2 - cyt. c_1 docking rather than a single conformation, all conformations exhibiting short heme edge-heme edge distances guaranteeing fast electron transfer; (iv) a lysine switch which attenuates interfacial adhesion after electron transfer; (v) a mobility mismatch between the cyt. c_2 and bc_1 complex binding surfaces that facilitates unbinding; (vi) a majority of the redox energy stored between the reduced and oxidized hemes being consumed for partner recognition and binding, rather than for driving electron transfer. These findings bridge the information gap between apparently conflicting experimental data over the past three decades, also providing a key example of interface recognition within a crowded cellular environment and its computational description.

Supplementary Material

Refer to Web version on PubMed Central for supplementary material.

Acknowledgments

References

1. Garrett, R., Grisham, C. Biochemistry. Cengage Learning; 2012.

2. Moser CC, Dutton PL. Biochemistry. 1988; 27:2450–2461. [PubMed: 2838074]

3. Fromme P, Melkozernov A, Jordan P, Krauss N. FEBS Lett. 2003; 555:40–44. [PubMed: 14630316]

4. Cartron ML, Olsen JD, Sener M, Jackson PJ, Brindley AA, Qian P, Dickman MJ, Leggett GJ, Schulten K, Hunter CN. Biochim. Biophys. Acta – Bioener. 2014; 1837:1769–1780.

5. Hunter, C., Daldal, F., Thurnauer, M., Beatty, J. The purple phototrophic bacteria. Vol. 28. Springer Science & Business Media; 2008.

6. Li Y, Naqui A, Frey TG, Chance B. Biochem. J. 1987; 242:417–423. [PubMed: 3036090]

7. Witt H, Malatesta F, Nicoletti F, Brunori M, Ludwig B. Eur. J. Biochem. 1998; 251:367–373. [PubMed: 9492306]

8. Geyer T, Helms V. Biophys. J. 2006; 91:927–937. [PubMed: 16714340]

9. Nyola A, Hunte C. Transactions. 2008; 36:981–985.

10. Solmaz SRN, Hunte C. J. Biol. Chem. 2008; 283:17542–17549. [PubMed: 18390544]

11. Guner S, Willie A, Millett F, Caffrey MS, Cusanovich MA, Robertson DE, Knaff DB. Biochemistry. 1993; 32:4793–4800. [PubMed: 8387815]

12. Venturoli G, Gabellini N, Oesterhelt D, Melandri BA. Eur. J. Biochem. 1990; 189:95–103. [PubMed: 2158893]

13. Long JE, Durham B, Okamura M, Millett F. Biochemistry. 1989; 28:6970–6974. [PubMed: 2554961]

14. Lange C, Hunte C. Proc. Natl. Acad. Sci. USA. 2002; 99:2800–2805. [PubMed: 11880631]

15. Sinjorgo KM, Steinebach OM, Dekker HL, Muijsers AO. Biochim. Biophys. Acta – Bioener. 1986; 850:108–115.

16. Axelrod HL, Abresch EC, Okamura MY, Yeh AP, Rees DC, Feher G. J. Mol. Biol. 2002; 319:501–515. [PubMed: 12051924]

17. Pietras R, Sarewicz M, Osyczka A. J. Phys. Chem. B. 2014; 118:6634–6643. [PubMed: 24845964]

18. Wang K, Zhen Y, Sadoski R, Grinnell S, Geren L, Ferguson-Miller S, Durham B, Millett F. J. Biol. Chem. 1999; 274:38042–38050. [PubMed: 10608873]

19. Kokhan O, Wraight CA, Tajkhorshid E. Biophys. J. 2010; 99:2647–2656. [PubMed: 20959106]

20. Paddock ML, Weber KH, Chang C, Okamura MY. Biochemistry. 2005; 44:9619–9625. [PubMed: 16008347]

21. Pelletier H, Kraut J. Science. 1992; 258:1748–1755. [PubMed: 1334573]

22. Volkov AN, Worrall JAR, Holtzmann E, Ubbink M. Proc. Natl. Acad. Sci. USA. 2006; 103:18945–18950. [PubMed: 17146057]

23. Hunte C, Koepke J, Lange C, Roßmanith T, Michel H. Structure. 2000; 8:669–684. [PubMed: 10873857]

24. Esser L, Elberry M, Zhou F, Yu C-A, Yu L, Xia D. J. Biol. Chem. 2008; 283:2846–2857. [PubMed: 18039651]

25. Kyndt JA, Fitch JC, Berry RE, Stewart MC, Whitley K, Meyer TE, Walker FA, Cusanovich MA. Biochim. Biophys. Acta – Bioener. 2012; 1817:811–818.

26. Tiede DM, Vashishta AC, Gunner MR. Biochemistry. 1993; 32:4515–4531. [PubMed: 8387335]

27. Autenrieth F, Tajkhorshid E, Schulten K, Luthey-Schulten Z. J. Phys. Chem. B. 2004; 108:20376–20387.

28. Roberts VA, Thompson EE, Pique ME, Perez MS, Ten Eyck L. J. Comp. Chem. 2013; 34:1743–1758. [PubMed: 23695987]

29. Jo S, Kim T, Im W. PLoS ONE. 2007; 2:e880. [PubMed: 17849009]

30. Jo S, Lim JB, Klauda JB, Im W. Biophys. J. 2009; 97:50–58. [PubMed: 19580743]

31. Wu EL, Cheng X, Jo S, Rui H, Song KC, Dávila-Contreras EM, Qi Y, Lee J, Monje-Galvan V, Venable RM, Klauda JB, Im W. J. Comp. Chem. 2014; 35:1997–2004. [PubMed: 25130509]

32. Jo S, Kim T, Iyer VG, Im W. J. Comp. Chem. 2008; 29:1859–1865. [PubMed: 18351591]

33. Brooks BR, et al. J. Comp. Chem. 2009; 30:1545–1614. [PubMed: 19444816]

34. Phillips JC, Braun R, Wang W, Gumbart J, Tajkhorshid E, Villa E, Chipot C, Skeel RD, Kalé L, Schulten K. J. Comp. Chem. 2005; 26:1781–1802. [PubMed: 16222654]

35. Klauda JB, Venable RM, Freites JA, O'Connor JW, Tobias DJ, Mondragon-Ramirez C, Vorobyov I, Alexander D, MacKerell J, Pastor RW. J. Phys. Chem. B. 2010; 114:7830–7843. [PubMed: 20496934]

36. Mackerell AD, Feig M, Brooks CL. J. Comp. Chem. 2004; 25:1400–1415. [PubMed: 15185334]

37. Autenrieth F, Tajkhorshid E, Baudry J, Luthey-Schulten Z. J. Comp. Chem. 2004; 25:1613–1622. [PubMed: 15264255]

38. Humphrey W, Dalke A, Schulten K. J. Mol. Graphics. 1996; 14:33–38.

39. Izrailev S, Stepaniants S, Balsera M, Oono Y, Schulten K. Biophys. J. 1997; 72:1568–1581. [PubMed: 9083662]

40. Izrailev S, Crofts AR, Berry EA, Schulten K. Biophys. J. 1999; 77:1753–1768. [PubMed: 10512801]

41. Isralewitz B, Baudry J, Gullingsrud J, Kosztin D, Schulten K. J. Mol. Graph. Model. 2001; 19:13–25. [PubMed: 11381523]

42. Conte LL, Chothia C, Janin J. J. Mol. Biol. 1999; 285:2177–2198. [PubMed: 9925793]

43. Crowley PB, Carrondo MA. Proteins: Struct., Func., Bioinf. 2004; 55:603–612.

44. Crowley PB, Ubbink M. Acc. Chem. Res. 2003; 36:723–730. [PubMed: 14567705]

45. Tanner DE, Chan K-Y, Phillips JC, Schulten K. J. Chem. Theor. Comp. 2011; 7:3635–3642.

46. Hunte C, Solmaz S, Lange C. Biochim. Biophys. Acta – Bioener. 2002; 1555:21–28.

47. Tetreault M, Rongey SH, Feher G, Okamura MY. Biochemistry. 2001; 40:8452–8462. [PubMed: 11456482]

48. Tetreault M, Cusanovich M, Meyer T, Axelrod H, Okamura MY. Biochemistry. 2002; 41:5807–5815. [PubMed: 11980484]

49. Becke AD. J. Chem. Phys. 1993; 98:5648–5652.

50. Kubota T, Yoshikawa S, Matsubara H. J. Biochem. 1992; 111:91–98. [PubMed: 1318882]

51. Gabellini N, Bowyer JR, Hurt E, Melandri BA, Hauska G. Eur. J. Biochem. 1982; 126:105–111. [PubMed: 6290210]

52. Sethi A, Eargle J, Black AA, Luthey-Schulten Z. Proc. Natl. Acad. Sci. USA. 2009; 106:6620–6625. [PubMed: 19351898]

53. Devanathan S, Salamon Z, Tollin G, Fitch JC, Meyer TE, Berry EA, Cusanovich MA. Biochemistry. 2007; 46:7138–7145. [PubMed: 17516628]

54. Charles Olea J, Kuriyan J, Marletta MA. J. Am. Chem. Soc. 2010; 132:12794–12795. [PubMed: 20735135]

55. Sener M, Strümpfer J, Singharoy A, Hunter CN, Schulten K. eLife. 2015 Submitted.

56. Kaila VRI, Johansson MP, Sundholm D, Wikstrom M. Proc. Natl. Acad. Sci. USA. 2010; 107:21470–21475. [PubMed: 21106766]

57. Mitin AV, Kubicki JD. Langmuir. 2009; 25:548–554. [PubMed: 19063621]

58. Atkins, P., de Paula, J. Atkins Physical Chemistry. OUP Oxford; 2010.

59. Yu C-A, Steidl JR, Yu L. Biochim. Biophys. Acta – Biomem. 1983; 736:226–234.

60. Krishnaswamy SR, Williams ER, Kirsch JF. Prot. Sci. 2006; 15:1465–1475.

61. Baker NA, Sept D, Joseph S, Holst MJ, McCammon JA. Proc. Natl. Acad. Sci. USA. 2001; 98:10037–10041. [PubMed: 11517324]

62. Battistuzzi G, Borsari M, Bortolotti CA, Di Rocco G, Ranieri A, Sola M. J. Phys. Chem. B. 2007; 111:10281–10287. [PubMed: 17685644]
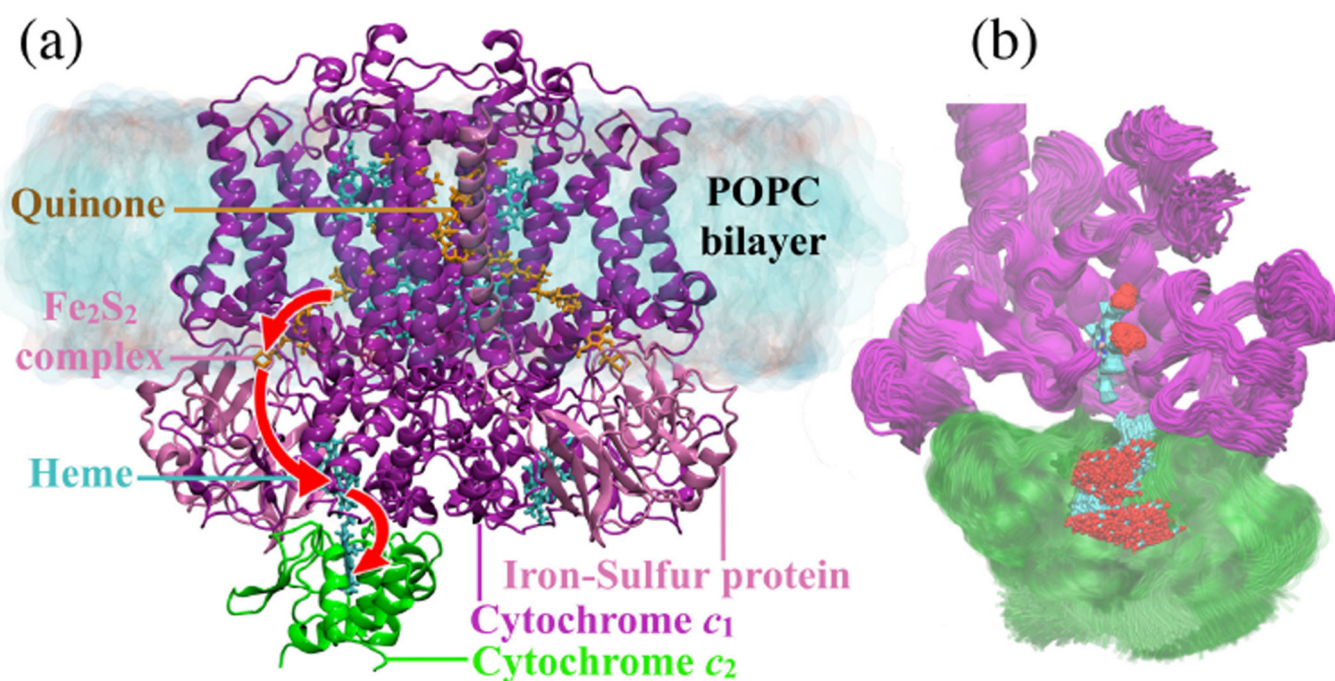
Figure 1. Structure of *Rba. sphaeroides* *bc*₁ complex embedded in lipid bilayer with bound cyt. c_2
(a) The cyt. *b* and cyt. c_1 subunits, one in each of the two monomers of the bc_1 complex, are shown in purple, cyt. c_2 in green, and the iron-sulfur protein subunit in pink. The putative electron transport pathway is indicated by red arrows. **(b)** Scatter diagram superimposing 10,000 structures (saved every 10 ps from the final 100 ns of the MD simulation of the DOT-docked model in the $c_2^O c_1^R$ state) reveal a conformational ensemble of cyt. c_2 bound to the cyt. c_1 subunit. The ensemble exhibits a distribution of heme-heme geometries, all with short edge-to-edge distances of 8.5 Å (Fig. 3a and Table S4). The distribution is representative of the thermal disorder at the binding interface. Purple: cyt. c_1 subunit of left bc_1 monomer; green: docked cyt. c_2; cyan: carbon atoms of cyt. c_1 and cyt. c_2 heme groups; red: oxygen atoms of the heme groups.
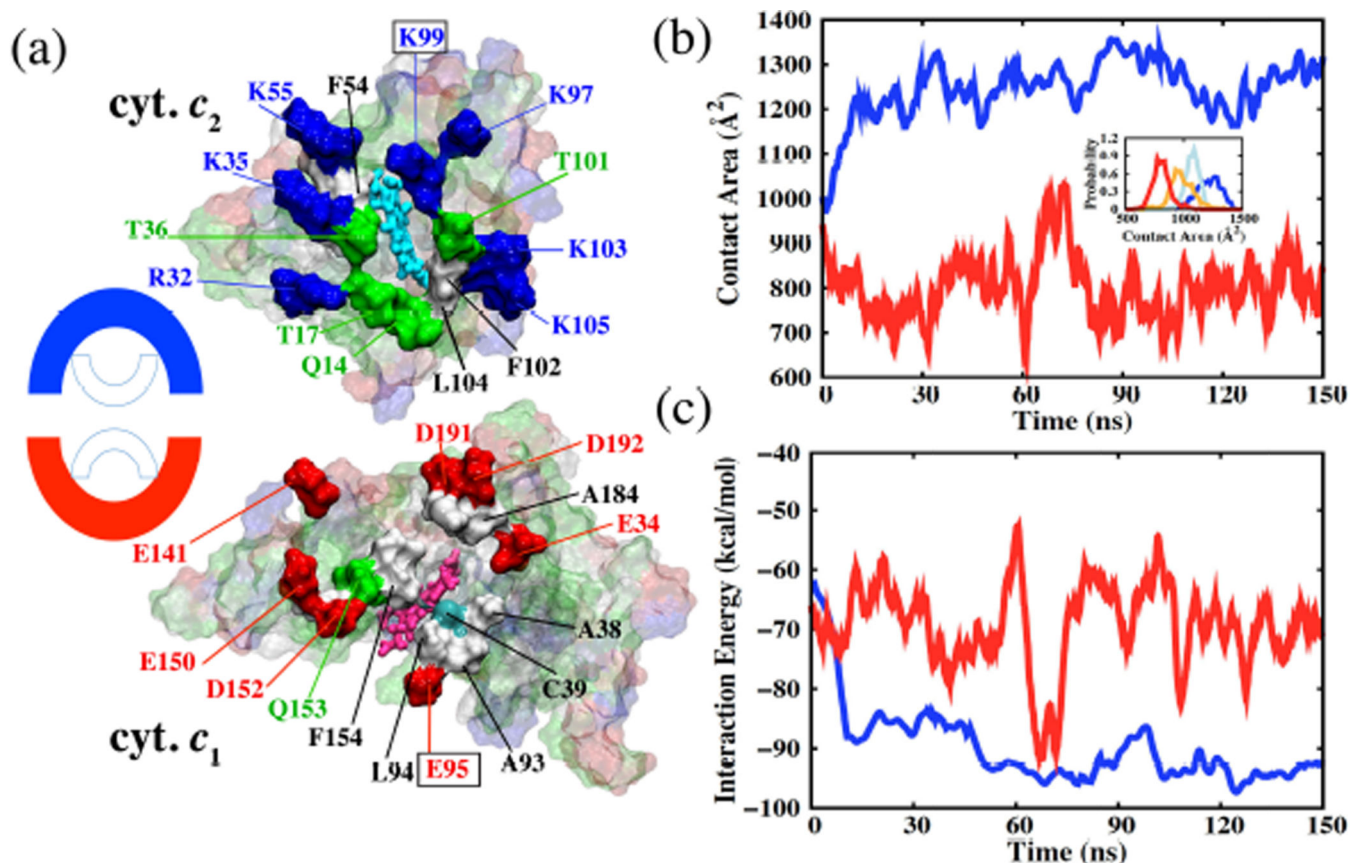
Figure 2. The cyt. c_2 - bc_1 complex interface in the pre-ET $(c_2^O c_1^R)$ state

(a) Complementarity of cyt. c_1 (bottom) and cyt. c_2 (top) surfaces. The two surfaces exhibit complementary outer half-rings of Glu and Asp (in cyt. c_1) and of Lys and Arg (in cyt. c_2) encasing an inner cluster of polar and hydrophobic residues. The outer half-rings attract each other into a fixed azimuthal orientation; the inner side groups add to the adhesion between cyt. c_2 and cyt. c_1 and provide an environment around the two heme groups that is conducive to electron transfer. The reduced cyt. c_1 heme is colored pink, the oxidized cyt. c_2 heme, cyan, the positively charged residues, blue, the negatively charged residues, red, the polar residues, green, and the non-polar residues, white. Residues shown in solid surfaces are selected based on their interface interactions as presented in Table 1. **(b)** Interface contact area of the cyt. c_2 - cyt. c_1 interface in redox states $c_2^O c_1^R$ and $c_2^R c_1^O$. While this area for the former, pre-ET, state on an average increases to 1200 c_2 over 150 ns of MD, the area of the latter, post-ET, state initially decreases and plateaus around 800 c_2. Inset: Contact area distribution over the MD trajectory showing that the area of $c_2^O c_1^R$ (blue) is larger than the area of $c_2^O c_1^O$ (light-blue), which is larger than the area of $c_2^R c_1^R$ (orange), and which is larger than the area of $c_2^R c_1^O$ (red). Structures were stored every ps to construct an ensemble of 1.5 $\times 10^5$ snapshots that are binned to obtain the distribution of physical properties of interest. **(c)** Interaction energy at the cyt. c_2 - cyt. c_1 complex. The increase in contact area of the interface in the pre-ET state is accompanied by a stronger cyt. c_2 - cyt. c_1 interaction,

implying relaxation of the docked model into an energy minimum; the post-ET cyt. c_2 - cyt. c_1 interface exhibits interactions that are attenuated by 20–30 kcal/mol.
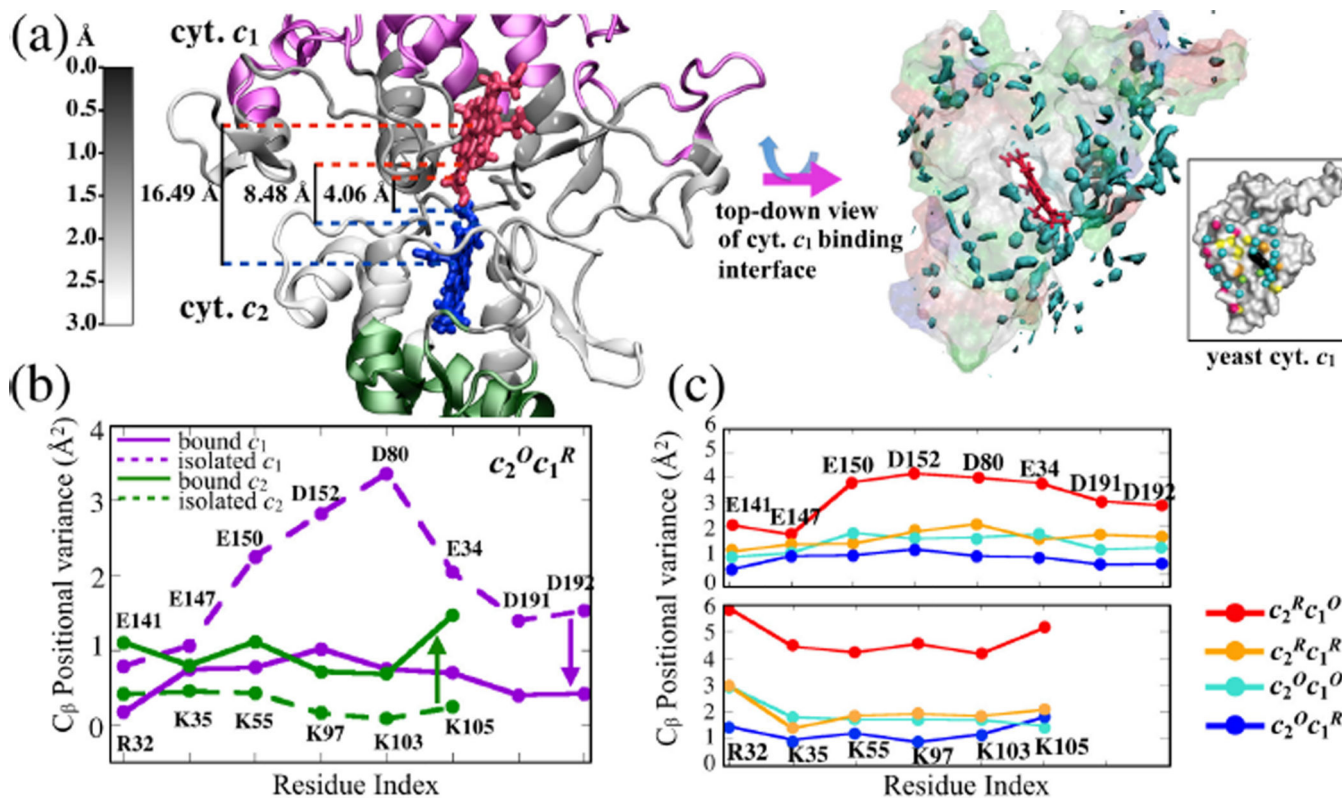
Figure 3. Redox state dependence of cyt. c_2 - bc_1 complex adhesion dynamics
(a) Interfacial residues of the cyt. c_2 - bc_1 complex are colored black to white based on the magnitude of backbone fluctuations relative to the initial structure, seen over the course of an MD simulation. The left figure shows that the bc_1 complex surface is less flexible than the cyt. c_2 surface. The inter-heme distances, as noted in Table S4, are labeled. A top-down view of the bc_1 complex on the right shows that its binding surface exhibits structured water. Presented is the water molecule density at a value of 50%. The water molecule density agrees very closely with that reported[10] for the yeast bc_1 complex (inset) supporting the accuracy of our docked model of the complex. (b) Positional variance of water-mediated electrostatically interacting residues as listed in Table 1a shows an increase in fluctuation for the cyt. c_2 surface residues (green) and a decrease for the bc_1 complex residues (purple) upon docking in redox state $c_2^O c_1^R$. Residues are labeled according to the order in Table 1a. (c) Effect of cyt. c_1 and cyt. c_2 redox states on dynamical properties of the adhesion complex. Presented is the positional variance of cyt. c_1 (upper panel) and cyt. c_2 (lower panel). The variance of the interface residues gradually increases from $c_2^O c_1^R$ (blue) to $c_2^O c_1^O$ (light-blue) to $c_2^R c_1^R$ (orange) to $c_2^R c_1^O$ (red). However, for a given redox state, variances in cyt. c_2 are greater than those in cyt. c_1. The strongest variance mismatch arises in changing the redox state to $c_2^R c_1^O$, namely for the redox state arising after electron transfer, when cyt. c_2 is supposed to separate from the bc_1 complex.
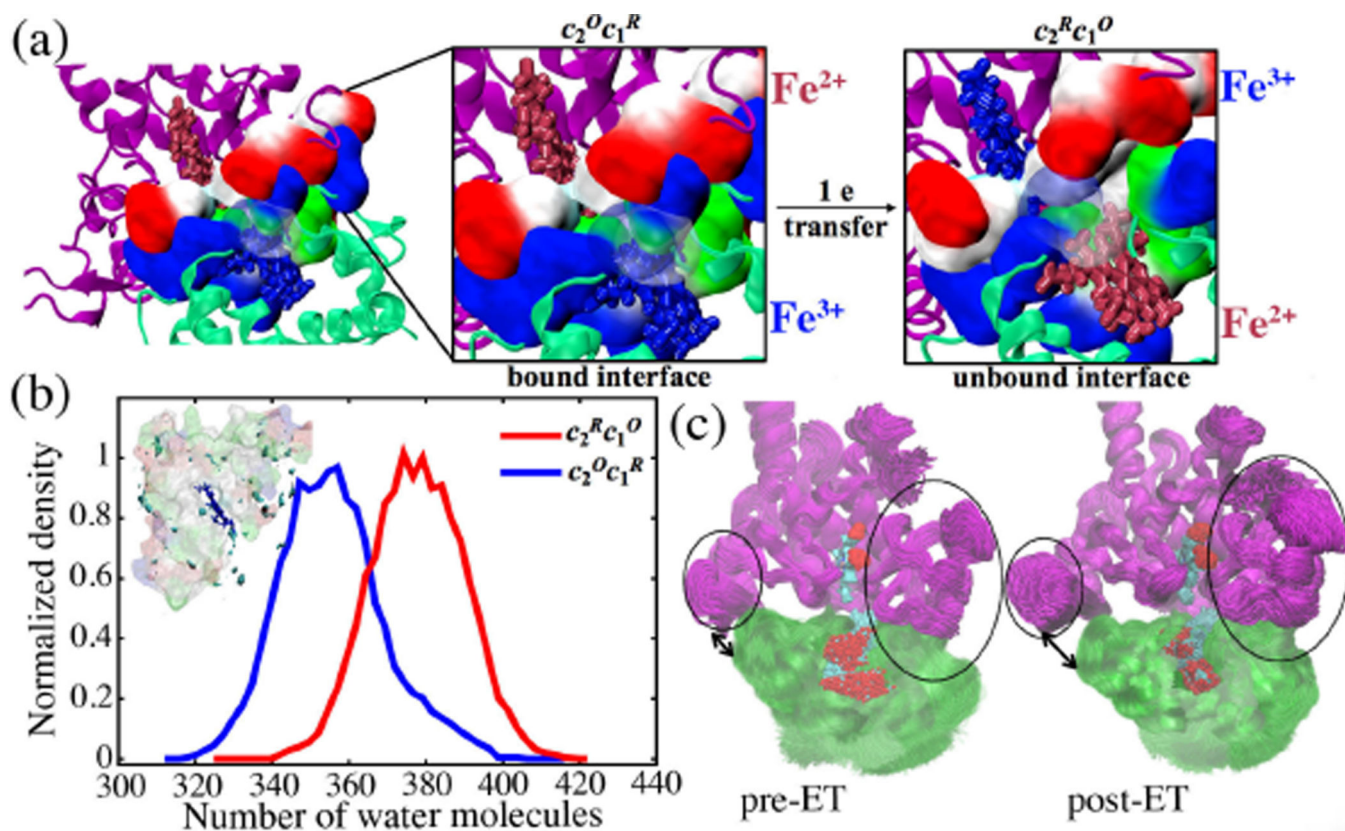
Figure 4. Cyt. c_2 - cyt. c_1 binding interface before $(c_2^O c_1^R)$ and after $(c_2^R c_1^O)$ electron transfer
(a) A loss of electrostatic interaction between positive cyt. c_2 residues (blue) and negative (red) cyt. c_1 residues can be inferred from the looser packing of the positive and negative residues. **(b)** Distribution of water molecules in the cyt. c_2 - cyt. c_1 interface. The number of water molecules increases in going from the pre-ET $(c_2^O c_1^R)$ to the post-ET $(c_2^R c_1^O)$ state. Inset: Occupancy of structured water is considerably less in the post-ET state than in the pre-ET state as also illustrated in Fig. 3a (inset). **(c)** Scatter diagram showing distributions of cyt. c_2 conformations on the bc_1 complex surface for the pre- and post-ET complex. The electron transfer renders the cyt. c_2 - cyt. c_1 interface less adhesive and more fuzzy as can be recognized by a larger interface-opening and stronger bc_1 complex scatter in the post-ET complex (see black ovals and black arrows). As in case of Fig. 1b, 10,000 structures are saved every 10 ps from the final 100 ns of the MD simulation (see Table S1) of the pre- and post-ET complex and superimposed here.
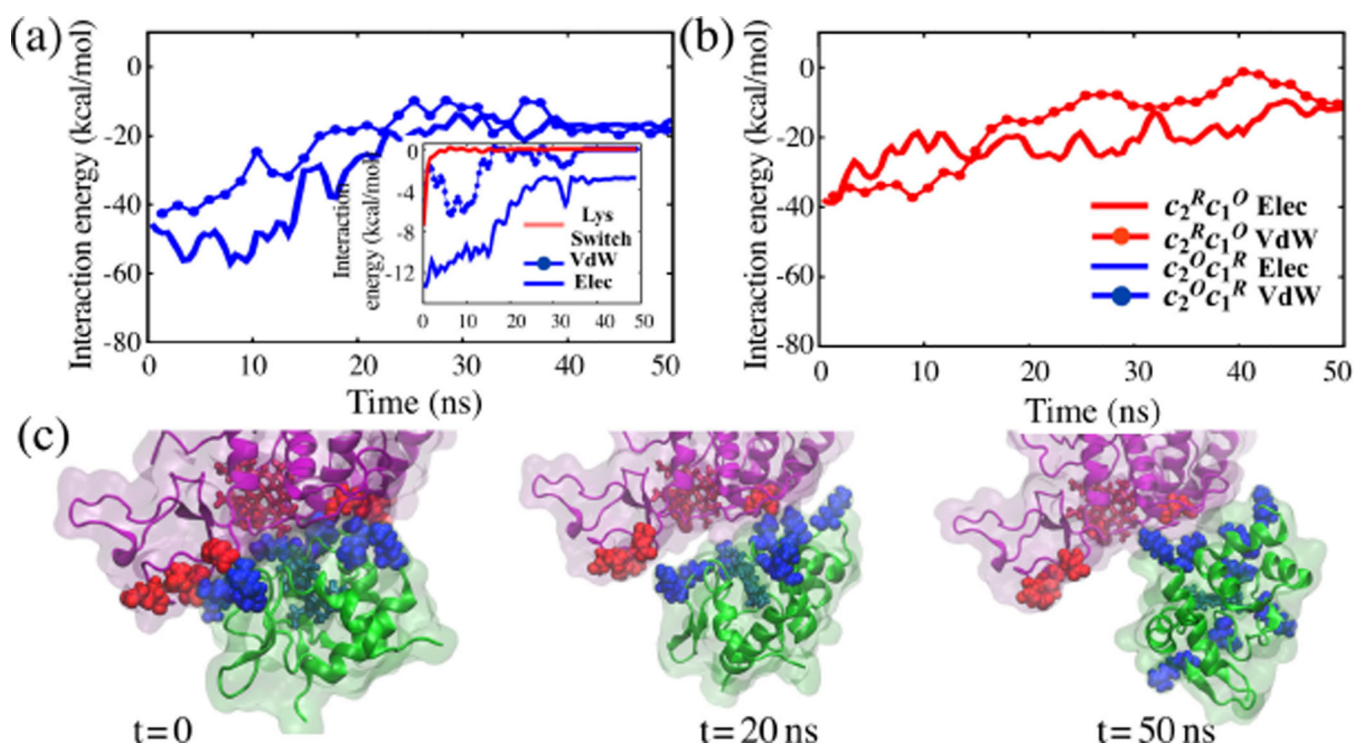
Figure 5. Analysis of steered MD simulations

Energy profile showing changes in the average interfacial van der Waals and electrostatic interactions during SMD simulations pulling apart the $c_2^O c_1^R$ **(a)** and $c_2^R c_1^O$ **(b)** complexes. Over the first 10–15 ns electrostatic interactions contribute more to adhesion in case of $c_2^O c_1^R$, while van der Waals interactions dominate in $c_2^R c_1^O$. Both interactions decrease with subsequent separation over the next 35–40 ns. Inset: Inter-residue interaction energies showing cyt. c_2 undocking is induced by the switching-off of the K99-E95 interactions (lysine-switch), which generally precedes destabilization of the hydrophobic interactions (QT14-M190 shown), ultimately followed by breaking of the water-mediated electrostatic interactions (K32-E41 shown). For simplicity, only select interactions are presented; more detailed results are provided in Fig. S3. **(c)** Cyt. c_2 undocking from bc_1 complex at $t = 0$, $t = 20$ ns and $t = 50$ ns showing most of the key interface stabilizing interactions subside within the first 20 ns of SMD simulations, after which cyt. c_2 unbinds from the bc_1 complex.
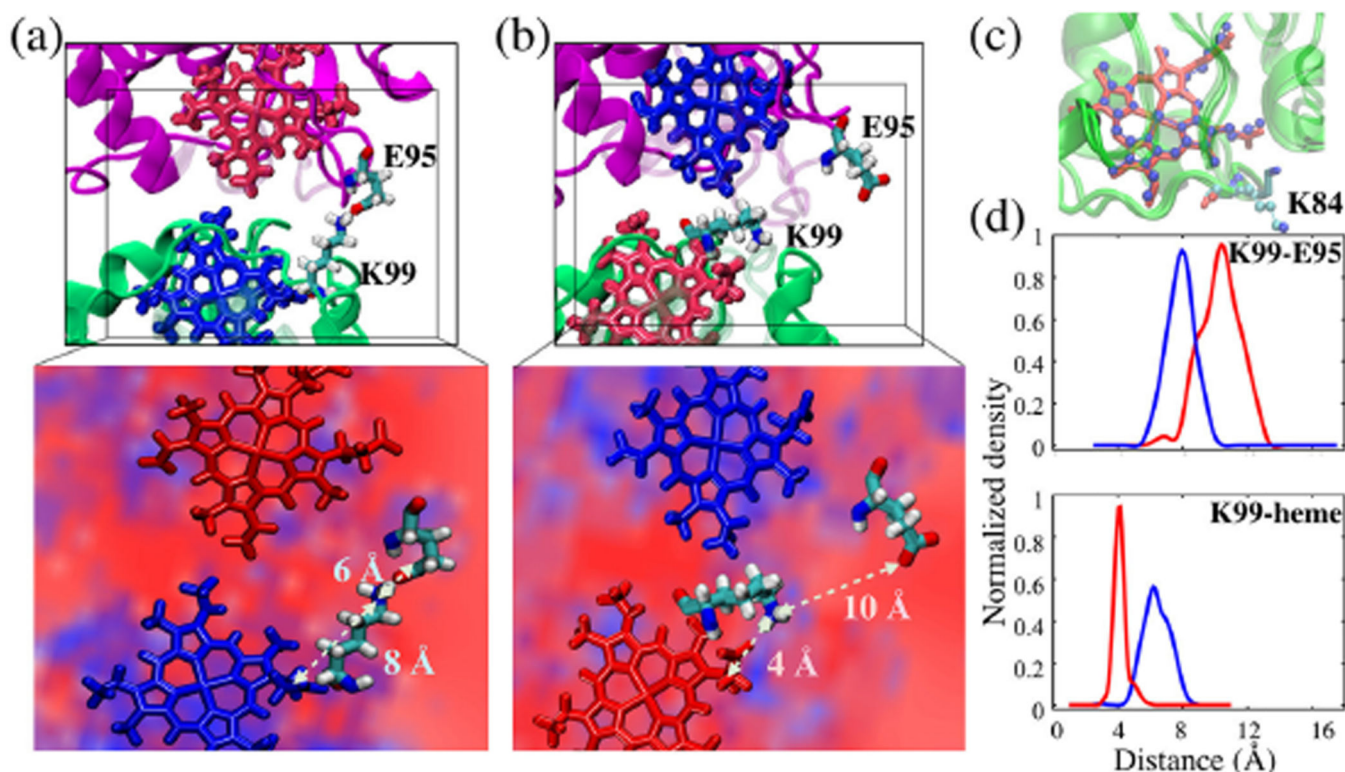
Figure 6. Lysine switch in cyt. c_2

Conformations of the K99 and E95 side-chains showing contact (switch on) in the $c_2^O c_1^R$ state **(a)** and no contact (switch off) after electron transfer in the $c_2^R c_1^O$ state **(b)**. Insets: Electrostatic potential isosurfaces of magnitude ± 10 kT/e in the vicinity of the lysine switch and the heme groups. The polarity of the field about the cyt. c_2 and cyt. c_1 hemes reverses with electron transfer. This reversal in polarity is visually indicated by the fact that the positive potential, lower left (blue background), in the vicinity of the oxidized cyt. c_2 heme (blue licorice) in **(a)** becomes negative, lower right (red background), after electron transfer when the heme becomes reduced (red licorice) in **(b)**, and vice-versa for the bc_1 complex. The electrostatic calculation was performed with a 1 Å grid using APBS.[61] **(c)** Evidence for a lysine switch due to interface residue K84 of yeast cyt. c is also seen in crystal structures, PDBID: 1KYO (CPK representation) and PDBID: 3CX5 (licorice). **(d)** Histograms showing that while the K99 - E95 distance (upper panel) increases after electron transfer from $c_2^O c_1^R$ (blue line) to $c_2^R c_1^O$ (red line), the K99-heme carbonyl distance (lower panel) simultaneously decreases.

Table 1

Interfacial interaction energies

Long-range (charged-charged), mid-range (charged-polar, charged-nonpolar, polar-polar) and short-range (polar-nonpolar, nonpolar-nonpolar) interaction energies between key residues at the cyt. c_2 - cyt. c_1 interface.

Energies are computed for pre- and post-ET states, employing a modified generalized Born (GB) model[45] with structures saved every picosecond from the final 100 ns of the MD simulations. The long-range interactions weaken in going from $c_2^O c_1^R$ to $c_2^R c_1^O$. Energy differences between the two redox states are highest for long-range electrostatic interactions, medium for mid-range interactions, involving polar residues, and smallest for short-range interactions involving non-polar residues.

(a) Long-range

cyt. c_2 - cyt. c_1	Interaction energy (Kcal/mol)	
	$c_2^O c_1^R$	$c_2^R c_1^O$
R32 - E141	−27.03±4.34	−5.26±2.16
R32 - E147	−1.47±0.52	0.00±0.14
K35 - E150	−11.42±3.12	−10.07±3.31
K35 - D152	−18.36±3.68	−1.20±0.54
K55 - D152	−7.70±2.15	−4.05±2.72
K95 - D80	−21.88±4.92	−4.73±2.98
K97 - E95	−20.68±3.47	−3.50±2.45
K99 - E95	−8.25±2.27	−3.12±2.41
K103 - E34	−16.60±3.76	−11.95±4.02
K105 - E34	−20.49±4.99	−9.82±4.12

(b) Mid-range

Q14 - D191	−4.17±1.68	−2.24±1.13
Q14 - D192	−2.30±0.92	−1.58±0.72
R32 - P142	−1.50±0.17	0.00±0.14
K35 - P151	−1.69±0.50	−0.86±0.21
T36 - Y155	−2.45±0.63	−1.20±0.53
F54 - D152	−1.42±0.32	−0.53±0.34
K97 - A93	−1.75±0.42	−0.45±0.31
T101 - C39	−2.26±0.35	−1.15±0.45

(c) Short-range

Q14 - M190	−2.88±0.32	−1.37±0.57
T17 - M190	−2.71±0.35	−2.05±0.72
T101 - A38	−3.85±0.67	−2.39±1.10
F102 - M190	−1.56±0.23	−1.23±0.27
F102 - L193	−3.22±0.23	−3.04±0.56

(c) Short-range		
*K35 - F154	−1.45±0.25	−1.43±0.36

*
denotes cation-π interactions.